International Journal of Thermophysics, Vol. 25, No. 4, July 2004 (© 2004)

Melting and Volume Vaporization Kinetics Effects in Tungsten Wires at the Heating Rates of 10^{12} to 10^{13} K/s[1]

A. D. Rakhel[2,3] and G. S. Sarkisov[4]

Experimental results on electrically exploded tungsten wires at the heating rates of 10^{12}–$10^{13}\,\mathrm{K \cdot s^{-1}}$ and their interpretation in the framework of a one-dimensional magneto-hydrodynamic model are presented. The effects of both melting and volume vaporization observed in these experiments are discussed. It is shown that superheating of solid tungsten does not take place at these heating rates (within a 10% experimental uncertainty). Some direct measurements performed in this study, and comparison of different quantities measured and calculated by the model, suggest that the volume vaporization starts close to a binodal line.

KEY WORDS: boiling; exploding wires; melting; resistivity; superheating; tungsten; vaporization.

1. INTRODUCTION

Kinetics of volume vaporization in electrically exploded wires has been discussed in the literature for a long time. Since the work of Bennett [1], it is usually assumed that the liquid phase is essentially superheated. Bennett developed a so-called vaporization wave model to describe the liquid–vapor phase transition caused by intense Joule heating. The model was based on the assumption that vaporization starts from the surface of a wire heated by an electrical current pulse and propagates to its axis as

[1]Paper presented at the Fifteenth Symposium on Thermophysical Properties, June 22–27, 2003, Boulder, Colorado, U.S.A.

[2]Institute for High Energy Densities, Izhorskaya 13/19, Moscow 125412, Russia.
[3]To whom correspondence should be addressed. E-mail: savlab@iht.mpei.ac.ru
[4]Ktech Corporation, Albuquerque, New Mexico 87106, U.S.A.

0195-928X/04/0700-1215/0 © 2004 Plenum Publishing Corporation

a wave. In the wave front the wire material undergoes a transition from the superheated liquid state to a two-phase liquid–gas state close to local thermodynamic equilibrium. The possibility of boiling in the bulk of the superheated liquid was considered to be less probable because the boiling kinetics and inertia effects in the two-phase mixture prevent such a scenario. The typical heating rates for experiments performed by Bennett are of the order of $10^9\,\mathrm{K}\cdot\mathrm{s}^{-1}$, which corresponds to a characteristic time of about $1\,\mu\mathrm{s}$ for an exploding wire residing in the liquid state.

Martynyuk [2] has introduced a hypothesis about the phase explosion to explain the exploding wire dynamics at these heating rates. It is assumed that a metal wire remains homogeneous during an initial stage of the heating process when the wire material is in a solid-state region and then in the liquid state before boiling begins. The boiling starts when the liquid reaches states close to a spinodal line. Such vaporization should behave like an explosion as the internal energy of the superheated liquid approaches the sublimation energy.

On the other hand, in the work [3] devoted to investigation of unloading of metals initially compressed by a shock wave, the start of boiling was clearly detected and used to determine the boiling curve position at high temperatures. In these experiments porous specimens were subjected to the shock compression and the velocity of the rear specimen surface was measured when the shock wave emerged at it. As a result of the volume vaporization, the velocity showed an additional increase in comparison with that for a superheated liquid. In this paper [3] a relaxation time for the volume vaporization was estimated to be on the order of 1 ns or even less.

Thus, the dynamic experiments were interpreted by the authors [1–3] using different points of view. It should be noted that no direct evidence of the remarkable superheating achieved in experiments [1, 2] is provided. The main goal of the present study is to find such evidence or to confirm the assumption [3] that the boiling starts close to the binodal line. The point is that the volume vaporization kinetics plays a very important role in the entire exploding wire dynamics [4]. For many applications a model should be developed describing the hydrodynamic flow caused by an exploding wire. This model should answer some specific questions, in particular, about the distributions of physical quantities across the plasma column formed by the wire [5, 6]. To answer the questions, the volume vaporization kinetics should be described correctly in such a model.

In the work of Ref. 4, a maximum heating rate of $10^{11}\,\mathrm{K}\cdot\mathrm{s}^{-1}$ was achieved. No superheating effects were detected in these experiments. Using the relaxation time for the volume vaporization of 1 ns from Ref. 3, one can obtain superheating of the order of 100 K for experiments [4], which is a very small value to be detected at the liquid tungsten

temperature of about 10 kK. It is of interest to answer the question: what is the heating rate that ensures maximum superheating, i.e., achievement of states close to the spinodal line? One may suppose that at this heating rate the temperature increases starting from the boiling point temperature T_b (P) to the spinodal temperature T_s (P) in 1 ns or less. In the case of tungsten one obtains a heating rate of about $7.7 \times 10^{12}\,\mathrm{K \cdot s^{-1}}$. In this estimate we used for the normal boiling point temperature of tungsten a value of 5830 K [7], and for the spinodal temperature a value of $T_s \approx 13,500$ K. The spinodal temperature was calculated by the van der Waals model and the value of T_s at zero pressure was used:

$$T_s(0) = \frac{27}{32} T_c, \tag{1}$$

where T_c is the critical temperature of tungsten ($T_c \approx 16,000$ K [4]).

The extremely high heating rates estimated above were used in the recent exploding wire experiments [8]. In this paper we present theoretical and experimental results of investigations of the exploding wire dynamics at heating rates of 10^{12} to $10^{13}\,\mathrm{K \cdot s^{-1}}$. Experiments with tungsten wires in air have been performed using the installation described in Ref. 8. The heating dynamics are described in the framework of a self-consistent one-dimensional magnetohydrodynamic (1D MHD) model [4, 9]. It is demonstrated that the model reproduces adequately (with a discrepancy less than 10%) all the dependences measured over the entire range of the heating rates. It is shown that both the melting and volume vaporization (boiling) start close to the corresponding equilibrium phase boundaries even at the maximum heating rates applied.

2. EXPERIMENTAL SETUP

A schematic diagram of the electrical circuit used is presented in Fig. 1. A 100 kV-Maxwell 40151-B pulse generator with a 6 nF capacitor bank and a 60 kV charging voltage provided an electrical current pulse. A 9 m long 50 Ω coaxial cable delivered the current pulse from the generator to a wire. The wire was placed in a coaxial target unit with four diagnostic windows. Figure 2 shows the coaxial target unit and the positions of a current and voltage detector. The downstream current through the wire was measured with a 2 GHz bandwidth 0.1 Ω coaxial-shunt resistor. The anode-ground voltage was measured with a V-dot (capacitive divider). A Si PIN-diode with a 1 ns rise time monitored the light emission power from the wire. All electrical waveforms were recorded with a 4-channel, 1-GHz digital scope, Tektronix TDS 684C. An SBS-compressed Nd:YAG

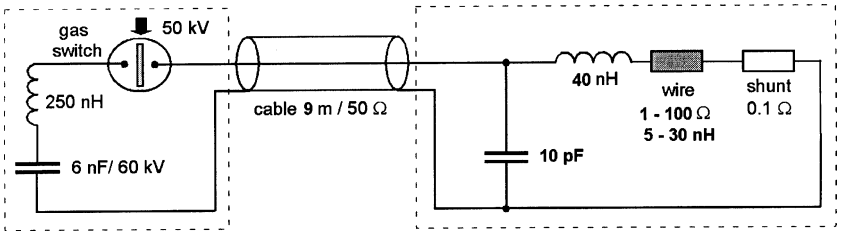

Fig. 1. Schematic diagram of electrical circuit.

Q-switch laser with 120 mJ energy at 532 nm and with 150 ps pulse duration (EKSPLA SL-312) was used for frame image shadowgraphy of the entire wire. Streak-camera (Hamamatsu C1587-01) radius–time diagrams of the exploding wire were obtained using a high-power pulse diode laser back lighter (Power Technology, IL30C, 905 nm, 10 W, 200 ns) and appropriate relay optics.

The experimental voltage waveform consists of resistive and inductive parts. For a fast current rate ($\sim 150\,\mathrm{A}\cdot\mathrm{ns}^{-1}$) experiment, it is important to calculate correctly the inductive voltage contribution to get a true value for the remaining resistive part. To get the inductance of the coaxial target unit, we measured the voltage waveforms for a shorted circuit, where a copper wire with a 3 mm diameter and 2 cm length was used in place of the specimen. The sample short circuit waveforms of the voltage, current, and a reconstructed inductive voltage $L_3\,dI/dt$ are presented in Fig. 3. For best fit for the inductive voltage, $L_3 \approx 50$ nH was obtained. The experimental curves presented in Fig. 3 demonstrate correctness of the measured current and voltage waveforms, as long as fairly good agreement between the inductive voltage $L_3 dI/dt$ and the measured voltage occurs. Here L_3 is actually the sum of the copper wire inductance L_{short} (~ 8.0 nH) and the target unit inductance. In our experiments with tungsten wires discussed below, the wire inductance was calculated by

$$L_{\mathrm{w}} = 2l\,\ln(D/d_0), \tag{2}$$

where l is the wire length, d_0 is its initial diameter, and D is the return current structure diameter (for the coaxial target unit used in our experiments, $D \approx 2.3$ cm). Equation (2) gives L_W in nH, when l, d_0, and D are in cm. The resistive voltage across the wire can be calculated by subtracting from the measured voltage the inductive voltage contribution $(L_{\mathrm{W}} + L_3 - L_{\mathrm{short}})dI/dt$.

All experiments in this study were carried out in air with tungsten wires having a diameter of 16.2 μm and a length of 2 cm. These wires were

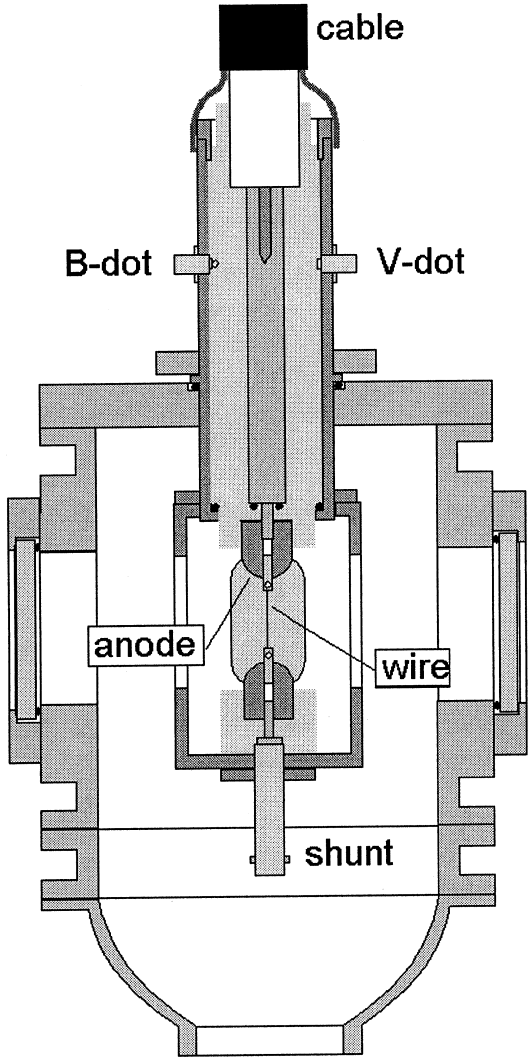

Fig. 2. Vacuum chamber with coaxial target unit.

manufactured by the California Fine Wire Company[5] with a specified purity of 99.95%.

[5]http://www.calfinewire.com

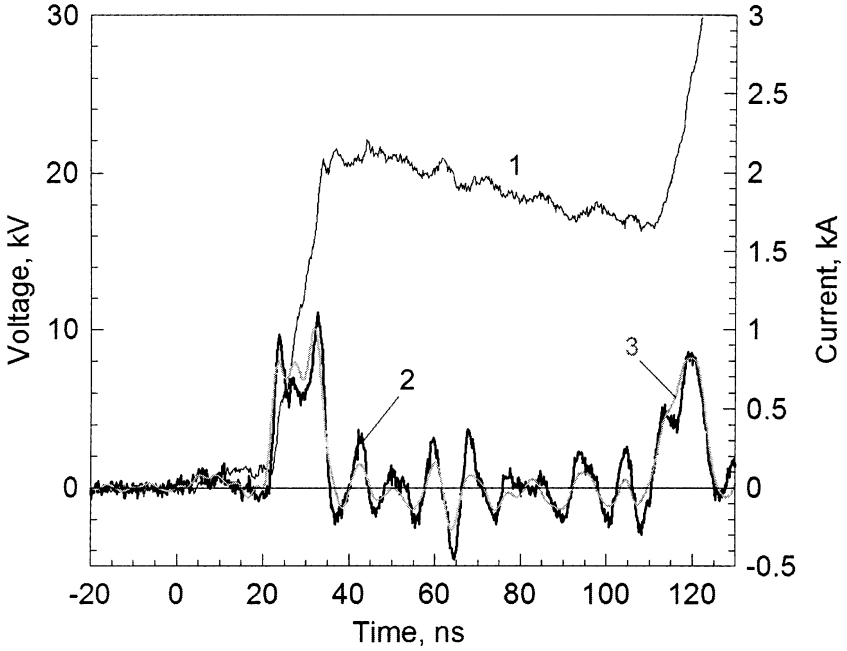

Fig. 3. Current (1) and voltage (2) waveforms measured for short circuit load. Inductive part of the calculated voltage (3) demonstrates good agreement with the measured voltage waveform.

3. ELECTRICAL CIRCUIT ANALYSIS

To investigate the kinetics effects in tungsten wires at heating rates up to $10^{13}\,\mathrm{K}\cdot\mathrm{s}^{-1}$, measurements of the current through the wire should be performed with high precision. It was a paramount task to determine the uncertainty of the current measurements. To solve this task, the shorted circuit current waveforms were calculated and compared with the measured ones.

Let us now discuss the approach used in these calculations. The pulser and the target unit were treated as quasistationary circuits since their geometrical dimensions are relatively small (of the order of 10 cm) while for the cable, telegraphic equations were solved. The current in the pulser circuit $I(t)$ satisfies the following equation:

$$\frac{d^2I}{dt^2}+\gamma_1\frac{dI}{dt}+\omega_1^2 I=0 \tag{3}$$

with $\gamma_1 = Z_2/L_1$, and $\omega_1 = 1/\sqrt{L_1 C_1}$, where L_1 is the pulser circuit inductance, C_1 is the capacitance of the capacitor bank, and $Z_2 = \sqrt{L_2/C_2}$ is the cable impedance. Here and below we designate index 1 for the pulser circuit parameters, 2 for that of the cable, and 3 for the target unit. The solution of Eq. (3) has a form,

$$I_1(t) \approx \frac{U_0}{\xi Z_2}\left[\exp\left(-\gamma_1^- t\right) - \exp\left(-\gamma_1^+ t\right)\right] \tag{4}$$

with $\gamma_1^+ = \gamma_1(1+\xi)$, $\gamma_1^- = \gamma_1(1-\xi)$, and $\xi = \sqrt{1-(2\omega_1/\gamma_1)^2}$, where U_0 is the charging voltage of the capacitor bank. In the case, the cable attenuation may be neglected, the following relation between the voltage U and the current magnitude I for the wave generated in the cable is valid: $U = \pm Z_2 I$, where the plus sign corresponds to the wave moving from the pulser to the target unit. The total current through the target unit is a superposition of the incident wave $I_i(t)$ and a reflected one $I_r(t)$, $I = I_i + I_r$. It can be shown that the total current through the target unit satisfies the following equation:

$$\frac{dI}{dt} + \gamma_3 I = 2\gamma_3 I_i(t), \tag{5}$$

where $\gamma_3 = Z_2/L_3$. In Eq. (5) the dependence $I_i(t)$ given by Eq. (4) should be used. The solution of Eq. (5) satisfying the initial condition $I(0) = 0$ is

$$I(t) = \frac{2U_0}{\xi Z_2}\left[\frac{\exp(-\gamma_1^- t) - \exp(-\gamma_3 t)}{1-\gamma_1^-/\gamma_3} - \frac{\exp(-\gamma_1^+ t) - \exp(-\gamma_3 t)}{1-\gamma_1^+/\gamma_3}\right]. \tag{6}$$

In Fig. 4 this temporal dependence is compared with the measured result (inductance L_1 was taken to be 250 nH). The solution given by Eq. (6) is valid only at times $t < t_2$, where t_2 is the instant of time when the second current wave reaches the target unit, i.e., the current wave reflected from the target unit and then from the pulser returns back. The interval of time between the neighbor current maxima in Fig. 4 is equal to the ratio of the double cable length to the wave velocity, i.e., $2l_2/\upsilon \approx 90$ ns, where $\upsilon = 1/\sqrt{L_2 C_2}$ and $l_2 = 9$ m (for the RG 220 cable used, $\upsilon \approx 20\,\mathrm{cm \cdot ns^{-1}}$).

On the basis of this comparison, we conclude that the electrical circuit used in our experiments has well defined parameters and the current measurements were performed with a precision better than 5% (as to the current magnitude). This is the reason why all the MHD computations presented below were carried out for prescribed temporal dependences of the current through the wire (these temporal dependences were taken from the corresponding experiments).

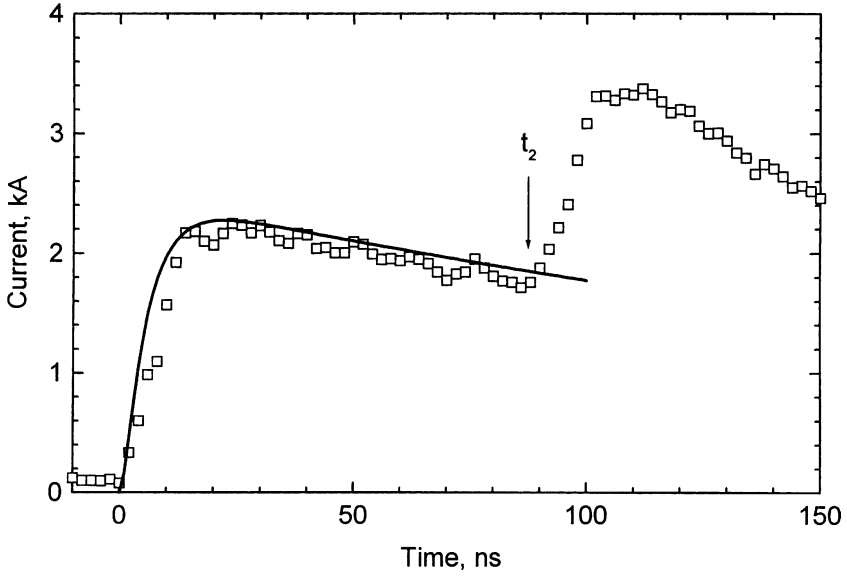

Fig. 4. Comparison of temporal dependences of the electrical current in shorted circuit: marks, experiment; solid line, analytical solution by Eq. (6).

4. MAGNETOHYDRODYNAMIC MODEL

To describe the hydrodynamic flow generated by a current pulse applied to a wire, the 1D MHD model [6, 9] was used. The corresponding set of equations of the model consists of the local laws of conservation of mass, linear momentum, and energy together with Maxwell's equations. It is assumed that the Z-pinch symmetry is maintained during the heating process. For the coordinate system the z-axis of which is directed along the axis of a wire, all physical quantities are functions of only the radius vector r and the time t. The only nonzero component of the velocity for this flow is the radial component. The electrical current density has a component only along the z-axis, and the magnetic field strength has only an azimuthal component.

It is easy to see that effects of the heat conduction, viscosity, and radiation may be neglected under these conditions, and therefore the corresponding terms were dropped in the equations of the model. The evaporation from the wire surface can be also neglected in this case, since this process is governed by the heat conduction from the bulk to the surface. Indeed, the characteristic time scale for the heat conduction is on the order of a^2/χ, where χ is the thermal diffusivity of tungsten and a is

the specimen radius. For $a = 8\,\mu$m and $\chi \approx 0.1$ cm$^2 \cdot$s^{-1} [10], we obtain a value of about $6\,\mu$s, what is much larger than the typical time scale for the heating process in our experiments (which is 10–30 ns).

The hydrodynamic flow was computed for two regions: the wire and surrounding air. We assumed that the substances do not mix with each other at the boundary. Thermodynamic functions of tungsten in the region of the liquid–vapor phase transition were obtained using an equation-of-state model from Ref. 11 with some modifications to better reproduce the behavior of the functions at high temperatures [4]. MHD computations performed in Ref. 4 have allowed the authors to establish the experimental conditions under which an expanding tungsten wire remains practically homogeneous down to a density of tungsten four times less than the standard solid density. These heating regimes were used to investigate the thermophysical properties of tungsten at substantially higher temperatures and pressures than those attained in slower experiments [12–14]. The fitting parameters of the EOS model were chosen [4] using these data.

Information on the electrical conductivity of tungsten in the liquid–vapor phase transition domain is also required for our computations. The basic idea of the approach to construct a conductivity dependence on the density and temperature in this domain is the following. In the condensed state (solid and liquid at low temperatures, $T < T_c$), the dependence was taken from experiments using an approximation of the experimental data obtained in Refs. 4, 9, and 12–14. In the gaseous state the conductivity was calculated using the approach presented in Ref. 15. In the intermediate region an interpolation was used. In the present work we focus on the liquid–vapor phase transition at pressures less than the critical pressure P_c (11 ± 2 kbar [4]). In this case one has no need for a detailed description of the electrical conductivity in the metal–nonmetal transition and the strongly coupled plasma region of the phase diagram. It is assumed that in the two-phase liquid–gas region the phases constitute a fine dispersed mixture. The conductivity of the mixture was calculated by means of the Landauer formula [16].

5. MELTING

Time-resolved waveforms of the current through the wire and the resistive part of the voltage drop across its length are presented in Fig. 5. The discrepancies between the calculated and measured voltages are less than 10% (in the time interval from 25 to 40 ns). The solid line for the current dependence in Fig. 5 represents a numeric approximation of the experimental data points and was used in the MHD computations as an input function. A laser shadowgram of the wire at the moment of time

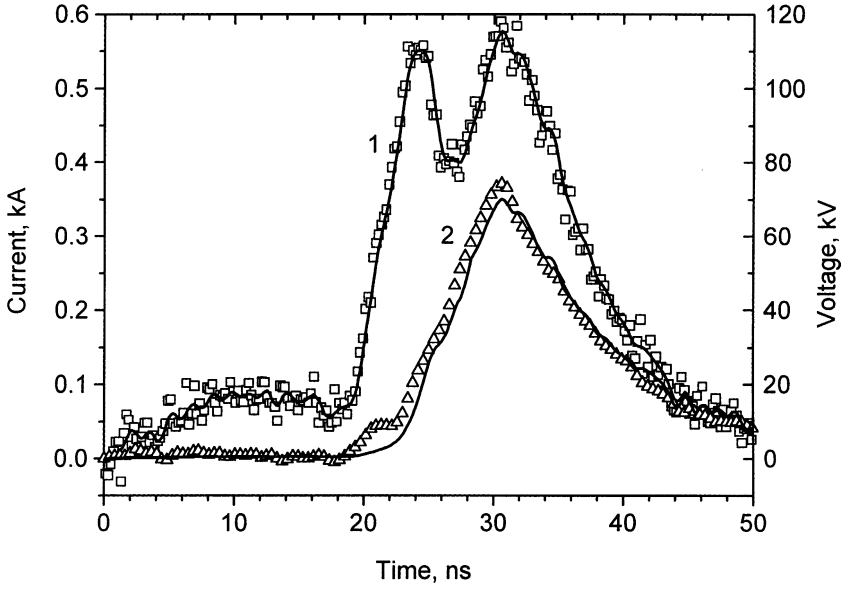

Fig. 5. Current through the wire (1) and resistive voltage drop across wire (2): marks, experiment; voltage solid line, modeling result; current solid line, numerical approximation of the experimental data points used in this modeling.

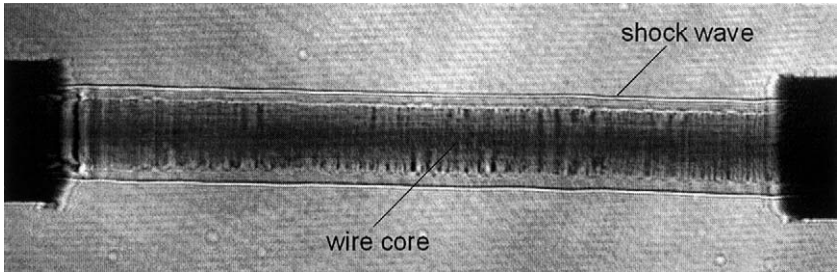

Fig. 6. Laser shadowgram of an exploding W wire of 16.2 μm diameter and 2 cm length at the moment of time $t = 1000$ ns from the voltage peak.

$t = 1000$ ns is presented in Fig. 6. As one can see, the column formed by the wire expands uniformly along the axial direction during a sufficiently long period of time. In the shadowgram an expanding wire core with a slightly perturbed boundary following a shock wave can be seen. The shock wave is uniform along the axial direction. Figure 6 demonstrates the validity of the assumption that the cylindrical symmetry is maintained during the process.

This paper deals primarily with vaporization kinetics effects. Nevertheless, the melting kinetics effects at the high heating rates applied in our experiments were also carefully investigated. The question about the melting kinetics can be formulated as follows: is it possible to observe the effects of superheating of the solid phase. Our approach was based on the well-known fact that the dependence of a tungsten wire resistance on enthalpy shows remarkable breaks at the beginning and end of melting [12–14]. The resistive voltage determined from our measurements was not sensitive enough to observe these features in the resistance versus specific enthalpy dependence. Therefore, the peculiarities were investigated in the dependences for the directly measured quantities: the current, the voltage, and the electrical heating power plotted as functions of the specific enthalpy.

In Fig. 7 the measured current through the wire and the electrical power input to it are shown as functions of the specific enthalpy. The electrical power is the product of the measured current through the wire and the resistive voltage across its length. The enthalpy was obtained by integrating the electrical power over time. It is obvious that there are two clear expressed breaks in the current dependence at the values of enthalpy that correlate with the solid- ($0.64\,\mathrm{kJ}\cdot\mathrm{g}^{-1}$) and liquid-phase enthalpy ($0.92\,\mathrm{kJ}\cdot\mathrm{g}^{-1}$) at the melting point [17]; the scatter of literature data with respect to these enthalpies is 6% [12–14, 17]. The electrical power exhibits a plateau in the melting region. Therefore, we can emphasize that there are no considerable shifts in the solid- and liquid-phase enthalpies at the melting point in comparison to the data obtained at the heating rates that are three orders of magnitude less. This demonstrates that no superheating (within 10% uncertainty) of solid tungsten is observed in our experiments[6].

It was important for observations of the features in the current and electrical power waveforms at melting to match the load and the pulser parameters properly. Only in experiments with the $16\,\mu$m in diameter and 2 cm long wires these features were manifested clearly enough to be detected.

In general, the effects of superheating should depend on the crystal structure of the specimen and, in particular, on the crystallite dimensions. What should be the average size of the crystallites such that the superheating is small? To answer the question we should make some estimates. The melting fronts starting at the crystallite boundaries are governed by the

[6]More accurate estimate of the superheating effect can be performed calculating the heat of fusion, i.e., difference between the enthalpies at the breaks. In this case the errors in determining the absolute values of the enthalpies will be compensated.

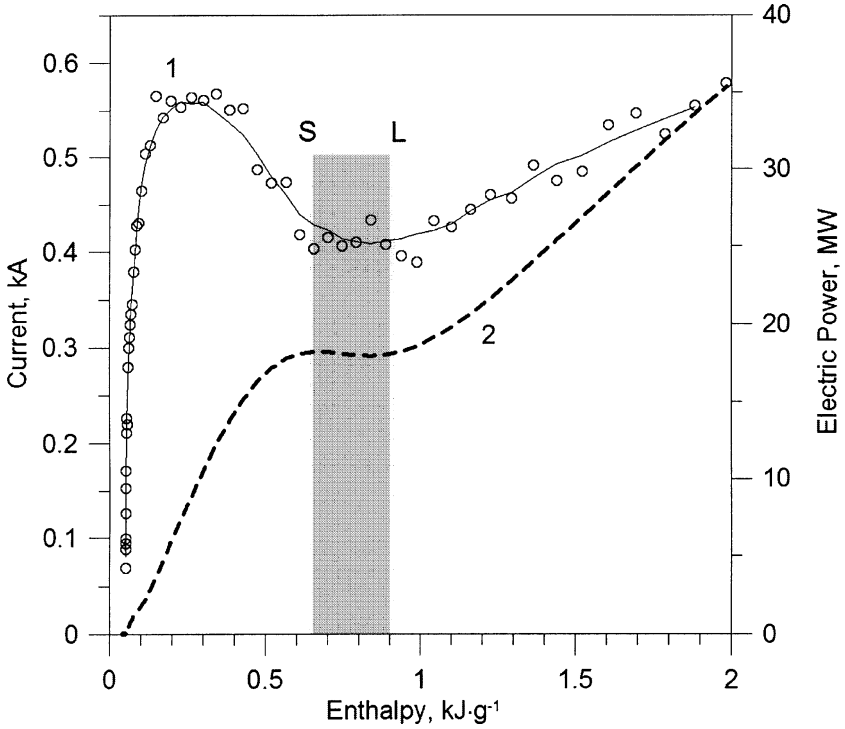

Fig. 7. Current through the wire (1) and electrical power input to wire (2) versus specific enthalpy. Grey area indicates the literature data for the solid (s) and liquid (l) state enthalpy at the melting point.

conduction transport. Therefore, if the average crystallite size is smaller than $2\sqrt{\chi t_m}$ (t_m is the melting duration), the superheating is small. For the experiment presented in Fig. 7, $t_m \approx 1$ ns and, therefore, the crystallites should be smaller than about $0.2\,\mu$m. Since the initial wire diameter is specified by the wire manufacturer with a precision of $0.1\,\mu$m, it is reasonable to conclude that the size of the crystallites in the tungsten wires utilized in the present work is $< 0.1\,\mu$m.

6. VAPORIZATION

Discussion of the vaporization kinetics is started from Fig. 8 in which the pressure and the so-called resistivity without the volume correction are shown as functions of the specific enthalpy. This resistivity (R^*) is a directly measured quantity and, on the other hand, it can be compared

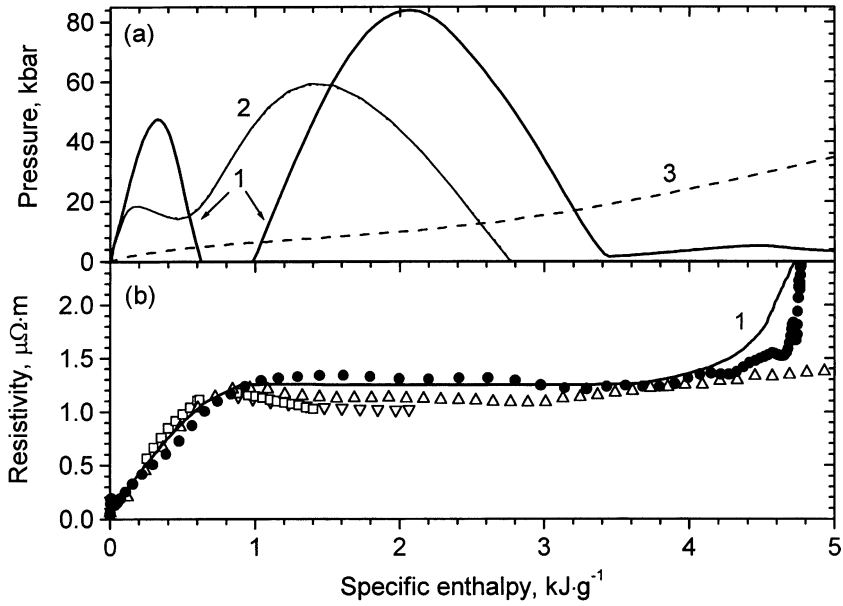

Fig. 8. Pressure (a) and resistivity without volume correction (b) versus specific enthalpy. Thick lines (1), modeling result for this work-experiment; thin line (2), pressure calculated by analytic formula, Eq. (9); dashed line (3), modeling result for an experiment reported in Ref. 9. Closed circles, this work-experiment; open triangles up [9]; triangles down [12]; squares [13].

with literature data. For the case when the specimen is heated homogeneously, this quantity is proportional to the ratio of the density ρ to the electrical conductivity σ,

$$R^* = \frac{1}{\sigma}\frac{\rho}{\rho_0} \tag{7}$$

(ρ_0 is the standard solid density).

As one can see in Fig. 8a, the pressure in the specimen (curve 1) does not vary monotonically; there are two maxima. This is a result of the temporal dependence of the Joule heating power having two maxima (which can be inferred from the current and voltage temporal dependences shown in Fig. 5). To explain the main features of the pressure behavior demonstrated in Fig. 8a, an analytical solution of the hydrodynamic equations for a wire subjected to pulse heating [18] can be used. The solution was deduced for the case $c_s t \gg a(t)$, where c_s is the speed of sound, $a(t)$ is the wire radius, and t is a characteristic time scale for the energy input. In this

case the density profile in the wire can be represented as a sum of a homogeneous term $\rho_h(t)$ depending only on time and a small inhomogeneous term $\rho'(r,t)$:

$$\rho(r,t) = \rho_h(t) + \rho'(r,t). \tag{8}$$

The pressure profile has the form,

$$p(r,t) \approx \frac{\rho_0 a_0^2}{2a}\frac{d^2a}{dt^2}\left[1-\left(\frac{r}{a}\right)^2\right], \tag{9}$$

where a_0 is the initial radius of the wire. The thin line in Fig. 8a corresponds to the pressure at the wire axis ($r = 0$) calculated by means of Eq. (9). In this calculation we used the temporal dependence of the Joule heating power as an input function. The following dependence of the liquid tungsten density versus specific enthalpy was used:

$$\rho = \rho_0(1-\alpha w), \tag{10}$$

where w is the specific enthalpy measured from the standard state and α is a constant which can be expressed through the thermal expansion coefficient and the heat capacity c_P($\alpha \approx 0.12\,\mathrm{g\cdot kJ^{-1}}$ [4]). Equation (10) was shown to be valid for solid and liquid tungsten in a wide density range [4]. The specific enthalpy as a function of time was determined from the measured current and voltage and was then used to obtain the derivative d^2a/dt^2, where the product $\rho_h(t)a(t)^2$ is a constant in this approximation. The difference between the Joule heat and the enthalpy is small under these conditions, and therefore, it can be neglected. As a result, the following expression can be obtained for the derivative (the radius acceleration):

$$\frac{1}{a}\frac{d^2a}{dt^2} = \frac{1}{2}\left[\frac{\alpha}{1-\alpha w}\frac{d^2w}{dt^2} + \frac{3}{2}\left(\frac{\alpha}{1-\alpha w}\frac{dw}{dt}\right)^2\right]. \tag{11}$$

As one can see, the pressure calculated by Eq. (9) shows qualitatively the same behavior as that obtained by means of the complete hydrodynamic model. Nevertheless, the absolute values of the pressure given by the analytical solution are remarkably lower. This is due to the importance of the delay effects under these conditions. Indeed, the acoustic time a/c_s is about 2 ns for the solid wire at room temperature and increases to about 6 ns for the melted wire at the normal boiling-point temperature; the value of the liquid tungsten sound speed at the normal boiling point is $2.5\,\mathrm{km\cdot s^{-1}}$ [14]. As follows from Fig. 5, the half width of the current peaks is comparable with the estimated acoustic time. Thus, the condition

$c_s t \gg a(t)$ is not valid. Therefore, one may not expect that the approach developed in Ref. 18 will provide quantitatively correct results in this case. The inertia effects are underestimated by Eq. (9). This is the reason why the difference exists in the timing of the maxima for the pressure curves calculated by Eq. (9) and that obtained by means of the 1D MHD model.

To show the contribution of the pinch effect, the magnetic pressure p_H was calculated:

$$p_H(r, t) \approx 10^{-3} Ij \left[1 - \left(\frac{r}{a}\right)^2\right], \tag{12}$$

where I is the current magnitude and j is the current density (SI units are used). Equation (10) was obtained for the quasistatic limit, i.e., when $c_s t \gg a$. In fact, the thin line presented in Fig. 8a is a superposition of two lines: the pressure obtained by Eq. (9) and the total pressure, i.e., the sum of the inertia pressure giving by Eq. (9) and the magnetic pressure by Eq. (12). It seems to be clear that the magnetic pressure can be neglected under these conditions.

The next important thing which can be inferred from Fig. 8 is a fairly good agreement between our measurements and those of Ref. 9. The pressure curves calculated for both these experiments intersect at an enthalpy of $3.1\,\mathrm{kJ \cdot g^{-1}}$. The corresponding values of the resistivity at this enthalpy practically coincide (to within the experimental uncertainty). Comparison of our data with those obtained in Refs. 12 and 13 should be performed at the same pressures that were used in the referenced studies. In experiments [12, 13] the pressures in the range of 2–5 kbar were applied to a wire-shaped specimen. In our experiment presented in Fig. 8, this low-pressure region was achieved only in a narrow enthalpy range of 0.6–$1.0\,\mathrm{kJ \cdot g^{-1}}$. As one can see, the resistivity curve for our experiment intersects the curves corresponding to Refs. 12 and 13 in just this enthalpy range.

Based on this comparison, two important features in the behavior of the tungsten resistivity under pressure have been revealed. As one can see in Fig. 8, in the solid-state region (at an enthalpy $< 0.64\,\mathrm{kJ \cdot g^{-1}}$) the resistivity measured in our experiment is lower than those measured at low pressures [9, 12, 13]. On the contrary, in the liquid-state region (at enthalpies $> 0.92\,\mathrm{kJ \cdot g^{-1}}$) our resistivity curve exceeds the low-pressure data. Therefore, we can conclude that the solid tungsten resistivity decreases with the pressure rise while the liquid tungsten resistivity increases remarkably when the pressure increases. Using the data obtained, the pressure derivative of the liquid tungsten resistivity $d\sigma^{-1}/dP$ was estimated to be of the order of $10\,\mu\Omega \cdot \mathrm{cm} \cdot \mathrm{GPa}^{-1}$ (at an enthalpy of $2.0\,\mathrm{kJ \cdot g^{-1}}$).

One remark should be done on the observations of the breaks in the dependence of the resistivity on the specific enthalpy at melting discussed

in Section 5. Due to the influence of pressure, these features were manifested clearly when the dynamic pressure at melting was low enough. As one can see in Fig. 8, this is the case for the 16 μm diameter wires.

The pressure evolution for this experiment at an enthalpy exceeding a value of 2 kJ $\cdot$ g^{-1} shows a continuing decrease followed by a plateau at 3.3 kbar. This plateau is formed when the substance enters the two-phase liquid–gas region and the boiling starts. The point is that the calculations were performed for the case when the boiling starts close to the binodal line. The resistivity measured in our experiment shows a rise very similar to that predicted by the model. It should be noted that the pressure line shown in Fig. 8a corresponds to the specimen axis; the boiling in the periphery regions starts earlier. Thus, the 1D MHD simulation results, assuming that vaporization starts close to the binodal line, are in good agreement with the experimental data.

To show another vaporization effect, we plot in Fig. 9 the temperature calculated for several radial layers in the specimen together with the measured light emission waveform. The layers represent only five cells of the spatial mesh among the 100–300 cells in the wire region used in our computations. Each layer contains a fixed mass of the substance, i.e., corre-

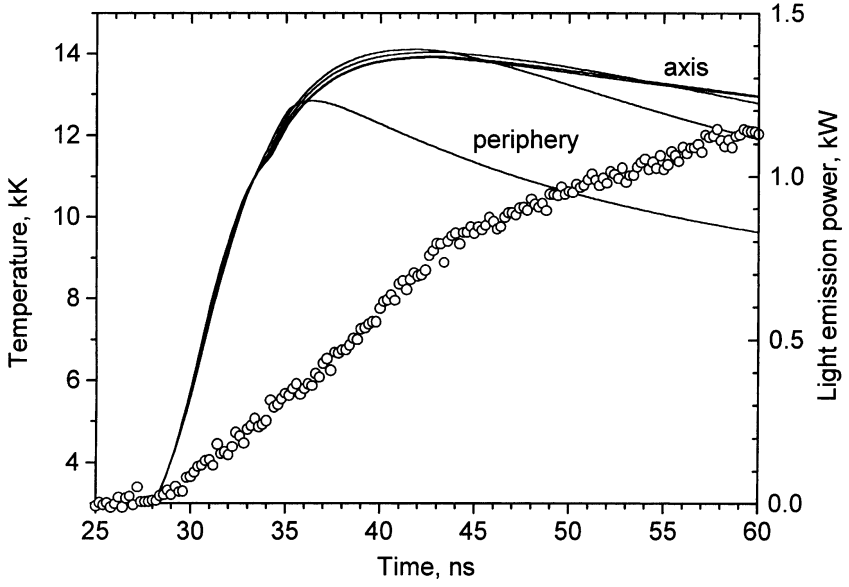

Fig. 9. Temperature calculated for several radial layers (lines) and the light emission signal measured (circles) as functions of time.

sponds to a specific Lagrangian coordinate. The clearly expressed break in the light emission signal correlates well with the maximum in the near-axis region temperature achieved at an instant of 42–43 ns. As the specimen diameter grows, the area from which the light is captured by the diode increases. Due to this the light emission signal increases even after the temperature at the near-axis region saturates. It appears that the peripheral layers in which the temperature decreases remarkably become transparent and the light emission from the inner regions is captured. The similar behavior for tungsten wires when a peripheral layer starts to boil and then becomes transparent has been discussed [4]. This behavior was used there to estimate the liquid core temperature where the pressure was high enough to prevent boiling.

A series of experiments was performed in this study to measure the wire diameter evolution. Streak image shadowgraphy was used. In Fig. 10 the calculated pressure at the wire axis (Fig. 10a) together with the measured wire radius (Fig. 10b) as functions of time are presented. The corresponding streak image of the wire is shown in Fig. 10c. It is obvious that the expansion observed in this experiment starts close to the onset of boiling predicted by the simulation. It should be noted that in this series of experiments an anode-ground breakdown was developed in several nanoseconds after the instant of time when the remarkable expansion starts. The breakdown was clearly detected in the voltage and the light emission waveforms. In spite of this breakdown problem, the streak image data demonstrate a reasonable correlation with the MHD simulation results. And furthermore, these direct measurements show that no essential superheating of liquid tungsten occurred. Since in the case of remarkable superheating, the expansion rate would remain low (as is observed for the liquid-state region) until the specific enthalpy approaches the sublimation energy (of about $4.6\,\mathrm{kJ}\cdot\mathrm{g}^{-1}$ [7]). For the experiment shown in Fig. 10, the specific enthalpy corresponding to the instance of time when the expansion starts is about $3.0\,\mathrm{kJ}\cdot\mathrm{g}^{-1}$.

7. CONCLUSIONS

It has been demonstrated that the exploding wire technique utilized in this work can be used for representative measurements at heating rates up to $10^{13}\,\mathrm{K}\cdot\mathrm{s}^{-1}$. It seems to be clear that the tungsten wires subjected to these heating rates can be rather accurately described in the framework of a 1D MHD model.

No remarkable shifts (within a 10% experimental uncertainty) of the solid and liquid phase enthalpy at the melting point were detected. This demonstrates that no essential superheating effects take place under these

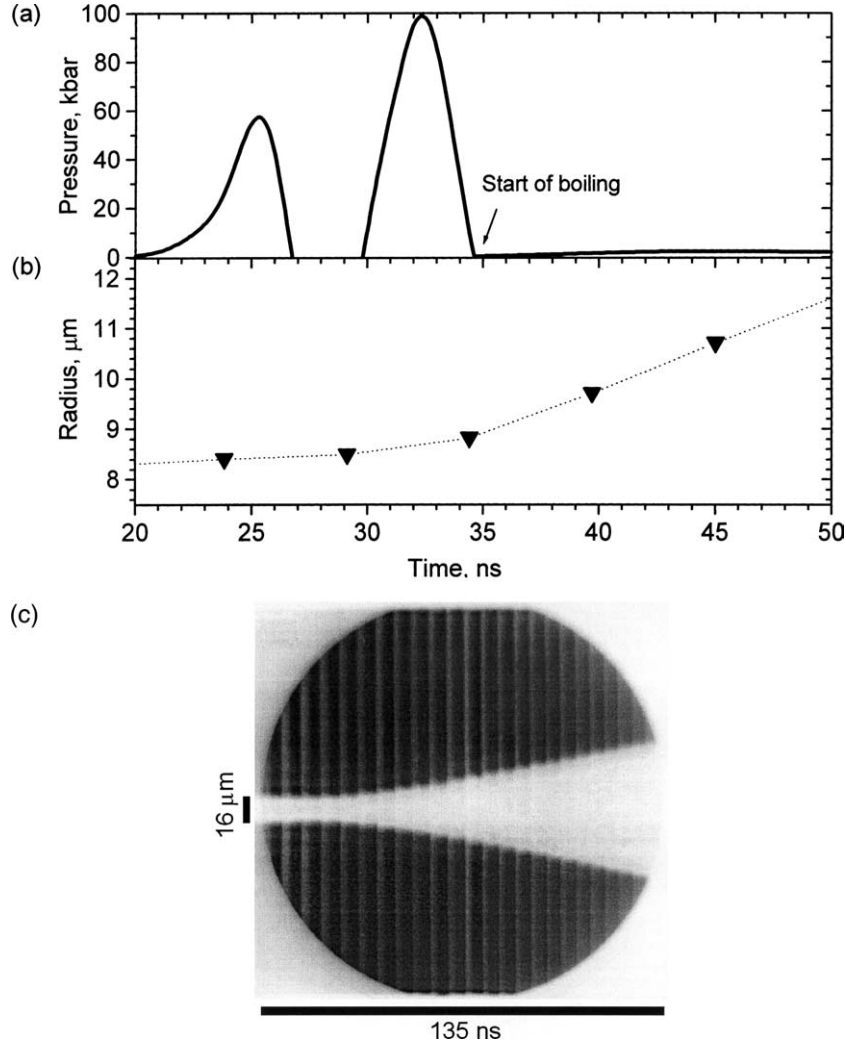

Fig. 10. Temporal dependences of the pressure at the (a) wire axis calculated; and the (b) wire radius measured; (c) streak image used for the radius measurement of a tungsten wire, 12 μm in diameter and 2 cm in length.

conditions. Some direct measurements performed in this study and comparison of different quantities measured and calculated by means the 1D MHD model have shown that the volume vaporization starts close to the binodal line.

ACKNOWLEDGMENTS

We thank Dr. Kenneth W. Struve for invitation for one of us (A. R.) to visit the Sandia National Laboratories and present the work at the Z-Pinch Physics and Power-Flow Department seminar. We thank Prof. Gernot Pottlacher, the chair of the Subsecond Thermophysics sessions at the 15th Symposium on Thermophysical Properties, for invitation to present the work as an invited paper.

REFERENCES

1. F. D. Bennett, in *Physics of High Energy Density*, Part 7, P. Caldirola and H. Knoepfel, eds. (Academic Press, New York and London, 1971).
2. M. M. Martynyuk, *Int. J. Thermophys.* **14**:457 (1993).
3. L. V. Altshuler, A. A. Bakanova, A. V. Bushman, I. P. Dudalapov, and V. N. Zubarev, *Zh. Eksp. Teor. Fiz.* **73:**1866 (1977).
4. A. D. Rakhel, A. Kloss, and H. Hess, *Int. J. Thermophys.* **23**:1369 (2002).
5. K. M. Chandler, D. A. Hammer, D. B. Sinars, S. A. Pikuz, and T. A. Shelkovenko, *IEEE Trans. Plasma Sci.* **30**:577 (2002).
6. A. W. DeSilva and J. D. Katsouros, *Int. J. Thermophys.* **20**:1267 (1999).
7. D. R. Lide and H. P. R. Frederikse, eds., *CRC Handbook of Chemistry and Physics* (CRC Press, Boca Raton, Ann Arbor, London, Tokyo, 1993–1994).
8. G. S. Sarkisov, P. V. Sasorov, K. W. Struve, D. H. McDaniel, A. N. Gribov, and G. M. Oleinik, *Phys. Rev. E* **66**:046413 (2002).
9. V. N. Korobenko, A.D. Rakhel, A. I. Savvatimskiy, and V. E. Fortov, *Plasma Phys. Repts.* **28**:1008 (2002).
10. H. Hess, A. Kloss, A. Rakhel, and H. Schneidenbach, *Int. J. Thermophys.* **20**:1279 (1999).
11. D. A. Young, *Lawrence Livermore Laboratory Report No. UCRL-52352* (1977).
12. U. Seydel, W. Fucke, and H. Wadle, *Die Bestimmung thermophysikalischer Daten flüssiger hochschmelzender Metalle mit schnellen Pulsaufheizexperimenten* (Verlag Dr. Peter Mannhold, Düsseldorf, 1980).
13. A. Berthault, L. Arles, and J. Matricon, *Int. J. Thermophys.* **7**:167 (1986).
14. R. S. Hixson and M. A. Winkler, *Int. J. Thermophys.* **11**:709 (1990).
15. V. V. Ermakov and N. N. Kalitkin, *Electron Transport in Dense Plasma* (Institute for Applied Mathematics, Moscow, 1977).
16. R. Landauer, *J. Appl. Phys*. **23**:779 (1952).
17. E. Arpaci and M. G. Frohberg, *Z. Metallkd.* **75**:614 (1984).
18. A. D. Rakhel, *Int. J. Thermophys.* **17**:1011 (1996).